

# Influence of Dynamic Compression on Phase Transformation of Martensitic NiTi Shape Memory Alloys



YING QIU, MARCUS L. YOUNG, and XU NIE

Shape memory alloys (SMAs) exhibit high damping capacity in both austenitic and martensitic phases, due to either a stress-induced martensite phase transformation or a stress-induced martensite variant reorientation, making them ideal candidates for vibration suppression devices to protect structural components from damage due to external forces. In this study, both quasi-static and dynamic compression was conducted on a martensitic NiTi SMA using a mechanical loading frame and on a Kolsky compression bar, respectively, to examine the relationship between microstructure and phase transformation characteristics of martensitic NiTi SMAs. Both endothermic and exothermic peaks disappear completely after experiencing deformation at a strain rate of  $10^3 \text{ s}^{-1}$  and to a strain of about 10 pct. The phase transformation peaks reappear after the deformed specimens were annealed at 873 K (600 °C) for 30 minutes. As compared to samples from quasi-static loading, where a large amount of twinning is observed with a small amount of grain distortion and fracture, samples from dynamic loading show much less twinning with a larger amount of grain distortion and fracture.

DOI: 10.1007/s11661-015-3063-5

© The Minerals, Metals & Materials Society and ASM International 2015

## I. INTRODUCTION

NiTi shape memory alloys (SMAs) have been extensively applied in civil,<sup>[1–3]</sup> medical,<sup>[4–8]</sup> and aerospace<sup>[9–11]</sup> devices for their unique shape memory effect, pseudoelasticity, bio-compatibility, and corrosion resistance.<sup>[12–18]</sup> The characteristic transformation temperatures for the austenite-to-martensite phase transformation as well as the mechanical response can be modified to meet application requirements through (i) thermo-mechanical processing,<sup>[19–21]</sup> (ii) slight variation from the equi-atomic NiTi chemical composition,<sup>[22,23]</sup> or (iii) addition of alloying elements.<sup>[24–28]</sup> This phase transformation generally involves an austenitic cubic B2 structure transforming to and from either a martensitic monoclinic B19 or orthorhombic B19' structure. Depending on the thermo-mechanical processing, intermediate phase transformations may occur as well; one of the particular notes is the commonly observed R-phase transformation, which involves a slight distortion of the austenitic cubic B2 structure.<sup>[13]</sup> Precipitates, such as Ni<sub>4</sub>Ti<sub>3</sub> in austenitic (Ni-rich) NiTi alloys and Ti<sub>2</sub>Ni in martensitic (Ti-rich) NiTi alloys, play a significant role in the concentration of Ni in small localized regions, which change the phase

transformation temperatures and mechanical properties. Although most dynamic investigations have been focused on austenitic NiTi alloys,<sup>[29–39]</sup> martensitic NiTi alloys also exhibit thermoelastic behavior and even better damping capacity,<sup>[40,41]</sup> due to the movement of twin interfaces. NiTi SMAs, which are fully martensitic at room temperature,<sup>[42]</sup> often have coarse brittle Ti<sub>2</sub>Ni precipitates. These precipitates can severely reduce the mechanical properties, lead to significant internal stresses at precipitate-matrix interfaces, and aid in crack propagation during loading.

Mechanical properties of martensitic NiTi SMAs under quasi-static loading have been extensively studied.<sup>[12,13]</sup> The martensite reorientation deformation proceeds in four stages: (I) elastic and homogeneous deformation of martensite, (II) propagation of localized reorientation bands (*e.g.*, twinning/detwinning), (III) elastic deformation of reoriented martensite, and (IV) plastic deformation (*e.g.*, slip). However, these distinct stages become difficult to observe especially during dynamic loading since two or more stages may be present locally at any given point in loading. After quasi-static compression loading, deformation bands and dislocations are generated in the martensite variant regions. Dislocation density increases dramatically, and the corresponding twinning system changes from  $\langle 011 \rangle$  type II twinning before deformation to  $(11\bar{1})$  type I twinning after deformation. There is no twin relation between neighboring martensite variants after compression because of the generation and movement of lattice defects.<sup>[43–46]</sup> The mechanical behaviors are nearly the same before the plastic deformation of reoriented martensite under quasi-static compression and dynamic compression, and the plastic stress level under dynamic

YING QIU, Ph.D. Graduate Student, is with the Materials Science and Engineering, University of North Texas, Denton, TX, and also with the Mechanical and Energy Engineering, University of North Texas, Denton, TX. MARCUS L. YOUNG, Assistant Professor, is with the Materials Science and Engineering, University of North Texas. Contact e-mail: marcus.young@unt.edu XU NIE, Assistant Professor, is with the Mechanical and Energy Engineering, University of North Texas.

Manuscript submitted November 17, 2014.

Article published online July 14, 2015

loading is 500 MPa higher than that under quasi-static compression.<sup>[47]</sup> NiTi SMAs also exhibit a dynamic sensitivity.<sup>[38,39,48]</sup> For martensitic NiTi SMAs, the deformation mechanism and microstructure are not sensitive to the strain rate within the range from 0.002 to 300 s<sup>-1</sup>.<sup>[49]</sup> The stabilization of the martensite under dynamic compression (strain rate: 1000 s<sup>-1</sup>) is similar as that under quasi-static compression.<sup>[47]</sup> However, the changes on microstructure and phase transformation features after dynamic compression, especially when the strain rate is higher than 1000 s<sup>-1</sup>, have not been fully investigated. In this paper, we examine the mechanical behavior of martensitic NiTi SMAs under dynamic compression when the strain rate is higher than 1000 s<sup>-1</sup>, and its recovery after annealing at various times and temperatures. Furthermore, we investigate the corresponding microstructural changes, phase transformation behavior, and structural variation after quasi-static loading and dynamic loading.

## II. EXPERIMENTAL METHODS

6.35-mm diameter rods (ATI Specialty Alloys and Components, Albany, Oregon) of binary NiTi SMA with 49.5 at. pct Ni were examined in this study. All samples were cut using an oil-cooled diamond wire saw (MTI Corporation, STX-202). After cutting, all samples were etched in a dilute nitric acid solution to remove the oxidized surface layer.

An FEI Nova 200 NanoLab and FEI Nova NanoSEM 230 scanning electron microscopy (SEM) with energy dispersive spectroscopy (EDS) were used to collect images and perform elemental analysis. A Netzsch DSC 204 F1 Phoenix differential scanning calorimeter (DSC) was used to measure the phase transformation temperatures. DSC samples with a mass between 10 and 50 mg were sealed in cold-weldable, lidded aluminum crucibles. The heating and cooling rate for the DSC experiments was 10 K/min. The samples were heated from room temperature [about 298 K (25 °C)] to 373 K (100 °C), held for 3 minutes to reach thermal equilibrium, cooled down to 173 K, held for another 3 minutes, and heated up again to 373 K (100 °C). Only the first cooling and second heating curves were used in this paper. X-ray diffraction (XRD) measurements were performed on Rigaku Ultima III X-ray diffractometer (XRD) operated at 40 kV and 44 mA with a CuK $\alpha$  radiation source. Diffraction patterns were recorded from 20 to 90 deg at a scanning rate of 1 deg/min. Dynamic compression experiments were conducted on a Kolsky compression bar at room temperature, as illustrated in the schematic in Figure 1. All compression samples had an aspect ratio 1:1, which was chosen to eliminate the influence of bending when the ratio is too large or the influence of barreling and friction at the contact surfaces when the ratio is too small under dynamic loading conditions. When setting the compression sample between the incident and transmission bars, grease (Dow corning high vacuum grease) is applied to both ends of the sample to reduce the end friction effect during compression testing. A pulse shaper, essentially a small piece of copper, is placed on the impact end of the incident bar to ensure that

constant strain rates and stress equilibrium are achieved under dynamic loading. As illustrated in the schematic in Figure 1, a single-loading momentum trap and screwed flange were also implemented in our Kolsky bar setup to facilitate precise deformation control as well as to ensure that the sample is not repeatedly loaded by the multiple wave reflections.<sup>[32,33]</sup>

For comparison with dynamic compression experiments, quasi-static compression tests were performed using a screw-driven material testing machine (Shimadzu, AG-IC 300 KN) at a strain rate of 10<sup>-3</sup> s<sup>-1</sup>. Strain control was based on the crosshead displacement. For direct comparison, the aspect ratio of the samples for quasi-static compression was also set to 1:1, which is identical to that for dynamic compression experiments. After dynamic compression loading, three subsequent heat treatments were performed on the deformed samples: (1) Annealing for 30 minutes at 573 K (300 °C), (2) Annealing for 30 minutes at 873 K (600 °C), and (3) Annealing for 30 minutes at 1123 K (850 °C). The first heat treatment was performed for the relaxation of the internal stresses after deformation and also to investigate the influence of low temperature annealing on the phase transformation temperatures. The second heat treatment was performed to reduce the phase transformation from a two-step to one-step phase transformation (*i.e.*, remove the R-phase transformation) by forming Ti<sub>2</sub>Ni precipitates which create a localized stress field that aids the phase transformation and improves damping capacity.<sup>[50,51]</sup> The third heat treatment was done to fully anneal the sample.

## III. EXPERIMENTAL RESULTS

An SEM image from the cross section of martensitic NiTi rod shows a martensitic NiTi matrix with dark particles (white arrow in Figure 2) which are evenly distributed and have a size ranging from 1 to 3  $\mu$ m, as illustrated in Figure 2(a). Based on three measurements from the matrix and the particles, respectively, the NiTi matrix consists of 50.80  $\pm$  0.06 at. pct Ni and 49.20  $\pm$  0.06 at. pct Ti, while the dark particle consists of 35.50  $\pm$  0.74 at. pct Ni and 64.50  $\pm$  0.74 at. pct Ti, which is consistent with Ti<sub>2</sub>Ni or Ti<sub>4</sub>Ni<sub>2</sub>O<sub>x</sub> particles, the later phase being more likely since it is more stable when forming an oxide.<sup>[42,52]</sup> Most of these particles are located at or near grain boundaries. After electropolishing for 2 minutes using 20 pct (by volume) H<sub>2</sub>SO<sub>4</sub> and 80 pct (by volume) CH<sub>3</sub>OH as an electrolyte, it can be seen that aligned martensitic twins are present in each grain and vary in direction depending on the specific grain orientation (as shown in Figure 2(b)).

The endothermic peak in the heating curve shows the combination of two types of phase transformation, and the peak fitting was conducted with Gaussian function to separate the two peaks from the heating curve. The dotted line is the best fit for martensitic phase transforming into R-phase, and the dashed line is the best fit for R-phase transforming into austenitic phase as shown in Figure 3. The start and finish temperatures of these two phase transformations are  $R_s = 335.6$  K (62.6 °C),

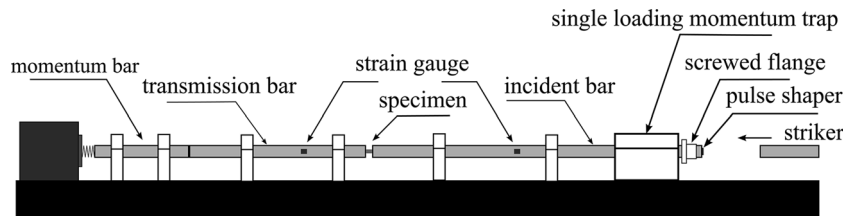


Fig. 1—Schematic diagram of Kolsky compression bar.

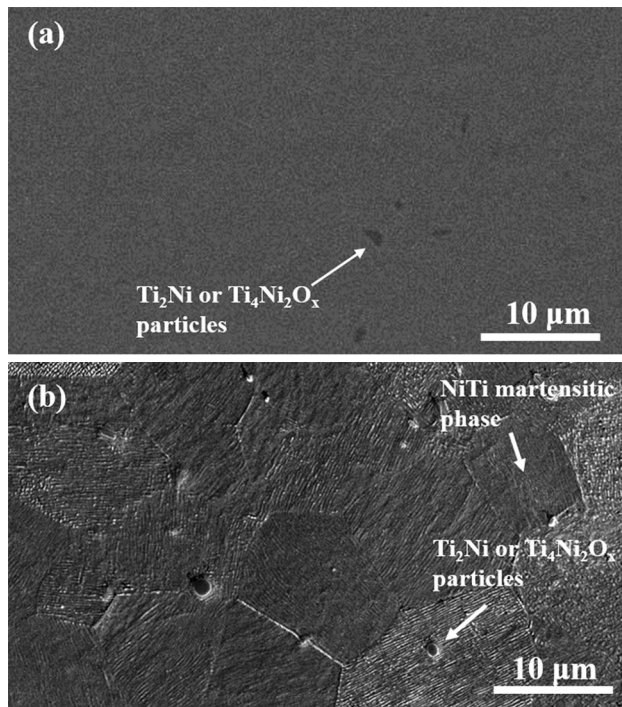


Fig. 2—SEM images of a hot-rolled martensitic NiTi SMA before compression testing and (a) before and (b) after electropolishing.

$A_s = 347.5$  K (74.5 °C), and  $R_f/A_f = 355.4$  K (82.4 °C), respectively. R-phase has a trigonal crystal structure, which can be obtained by elongating the cubic lattice (austenite phase) along  $\langle 111 \rangle_{B2}$  direction.<sup>[13]</sup> R-phase is a commonly observed intermediate phase in NiTi alloys which can result from cold working or heat treating.<sup>[53]</sup> The R-phase transformation occurs between austenite and martensite during cooling or mechanical loading.<sup>[54]</sup> The exothermic peak in the DSC cooling curve of the martensitic NiTi SMA indicates a martensite start [ $M_s = 324$  K (51.4 °C)] and finish [ $M_f = 311.8$  K (38.8 °C)] temperatures.

The heating and cooling DSC curves for the martensitic NiTi SMA in the (a) as-received hot-rolled state, (b) after dynamic loading, (c) after dynamic loading and annealing for 30 minutes at 573 K (300 °C), (d) after dynamic loading and annealing for 30 minutes each at 573 K and then 873 K (300 °C and then 600 °C), (e) after dynamic loading and annealing for 30 minutes each at 573 K (300 °C), then 873 K (600 °C), and finally 1123 K (850 °C), and (f) after heat treatment of non-deformed as-received specimen for 30 minutes at 1123 K (850 °C) are shown in Figure 4. No heat

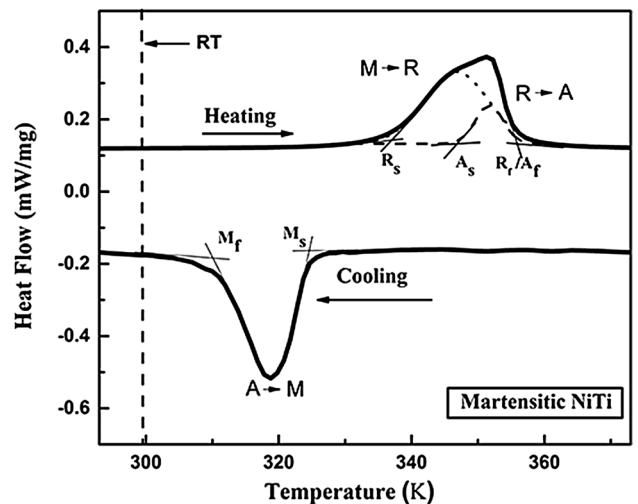


Fig. 3—DSC curves for the as-received hot-rolled martensitic NiTi before compression.

treatments were performed before dynamic compression to avoid forming brittle and coarse  $Ti_2Ni$  or  $Ti_4Ni_2O_x$  particles, which are commonly observed in martensitic NiTi SMAs after heat treatment. Two-step B19'-R-B2 transformation on heating and one-step B2-B19' on cooling with a hysteresis of 32 K (32 °C) were observed for the martensitic NiTi (Figure 4(a)). The two-step phase transformation peaks upon heating overlap with each other, so it is difficult to distinguish them without careful comparison. X-ray diffraction results, which will be presented later in the text, support that these transformation peaks correspond to B19' and B2. Although R-phase was not observed in X-ray diffraction patterns due to its instability at room temperature, the peak which appears before the austenite peak during cooling is typical of R-phase and is assumed to be R-phase here.<sup>[13,53,54]</sup> After dynamic compression, phase transformation peaks on both heating and cooling curves disappeared completely (Figure 4(b)). Although not shown here, even with extending the temperature to 423 K (150 °C) on heating and 123 K (-150 °C) on cooling, no phase transformation peaks were observed. DSC of quasi-statically loaded samples also showed that the phase transformation peaks disappeared at stress levels above 1500 MPa or 9 pct strain. The details of the data are, however, not presented here since it is beyond the scope of this research. After the deformed sample was annealed at 573 K (300 °C) for 30 minutes, a small peak with very low amplitude appeared during heating at about 328 K (55 °C), while the cooling curve showed

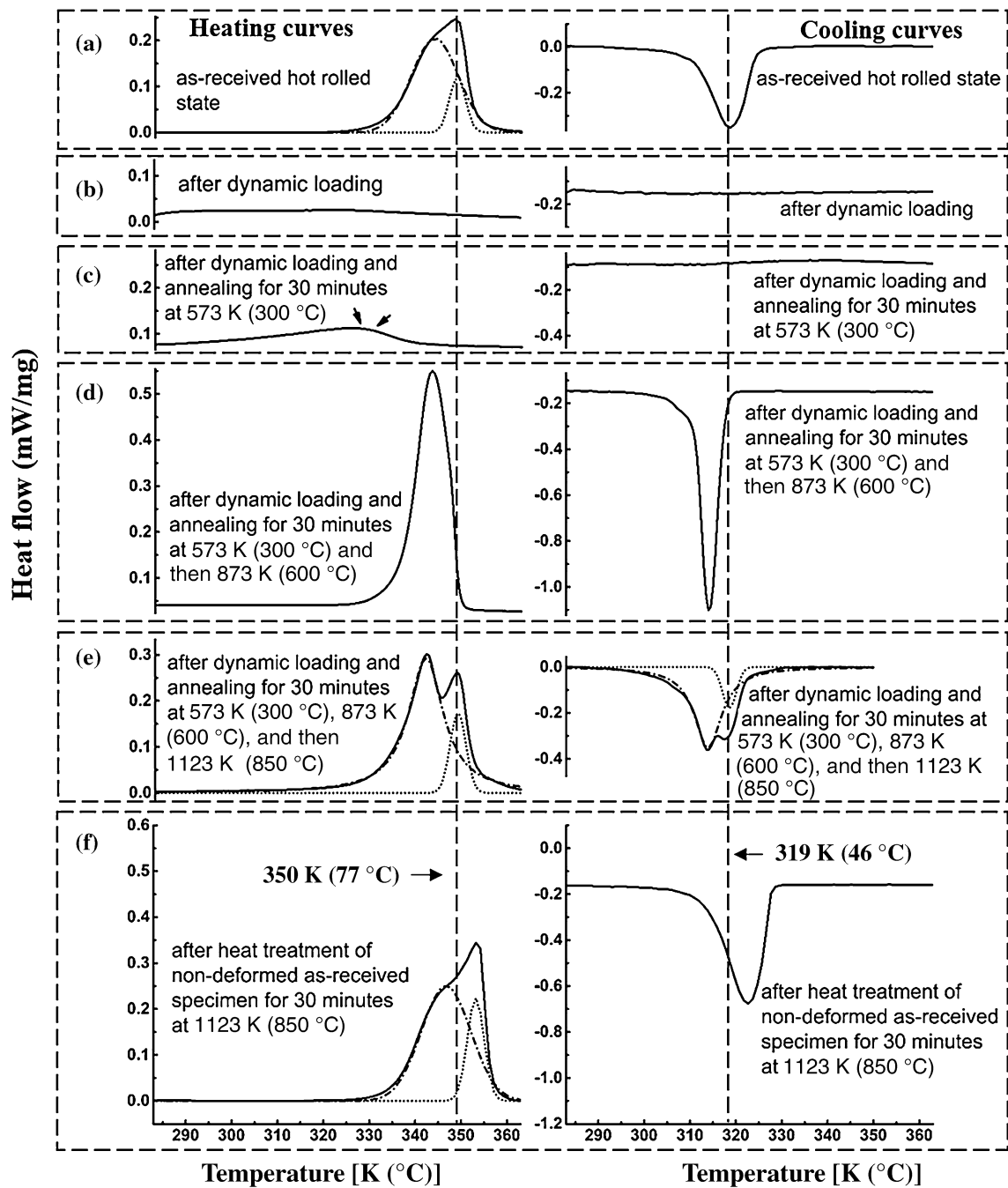


Fig. 4—Heating and cooling DSC curves for martensitic NiTi SMA in the (a) as-received hot-rolled state, (b) after dynamic loading, (c) after dynamic loading and annealing for 30 min at 573 K (300 °C), (d) after dynamic loading and annealing for 30 min each at 573 K (300 °C) and then 873 K (600 °C), (e) after dynamic loading and annealing for 30 min each at 573 K, 873 K, and then 1123 K (300 °C, 600 °C, and then 850 °C), (f) after heat treatment of non-deformed as-received specimen for 30 min at 1123 K (850 °C).

no evidence of peaks, *i.e.*, no phase transformation (Figure 4(c)). As illustrated in Figure 4(d), when the sample was subsequently annealed again at 873 K (600 °C) for another 30 minutes, two sharp peaks were observed with a slight shift down from the initial hot-rolled state peak values (350 K (77 °C) on heating and 319 K (46 °C) on cooling). Finally, the sample was annealed again at 1123 K (850 °C) for 30 minutes, and two peaks were observed during both heating and

cooling (Figure 4(e)), which is consistent with two-step B19'-R-B2 transformation. For comparison, a sample was heat treated at 1123 K (850 °C) for 30 minutes. Similar to the peaks observed in Figure 3, an overlapping two-step phase transformation is observed during heating of the as-received hot-rolled state samples (Figure 4(a)), after dynamic loading and annealing for 30 minutes at 573 K (300 °C), then 873 K (600 °C), and finally 1123 K (850 °C) (Figure 4(e)), and after heat

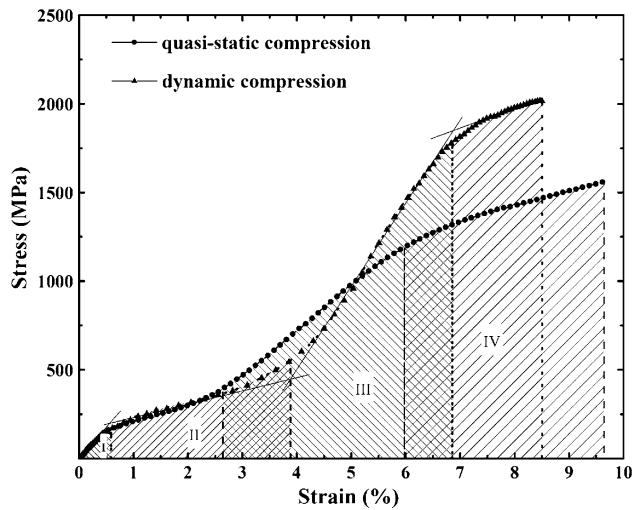


Fig. 5—True stress-strain curves of martensitic NiTi under dynamic compression (triangle line) and quasi-static compression (dot line) at a strain rate of 1500 and  $10^{-3} \text{ s}^{-1}$ , respectively.

treatment of non-deformed as-received specimen at 1123 K (850 °C) for 30 minutes (Figure 4(f)). Peak fitting was conducted as described above. No apparent peak shifts have been observed on both  $M \rightarrow R$  type and  $R \rightarrow A$  type phase transformation after dynamic loading and the following heat treatment except that these two peaks became sharp; however, both phase transformation peaks shift +5 K (+5 °C) toward high-temperature direction after the sample was heated at 1123 K (850 °C) for 30 minutes. Therefore, the phase transformations remain in the same peak position after dynamic loading and annealing for 30 minutes at 573 K (300 °C), 873 K (600 °C) and then 1123 K (850 °C) (Figure 4(e)) as compared to as received hot-rolled state (Figure 4(a)), whereas the sample after only heat treatment for 30 minutes at 1123 K (850 °C) (Figure 4(f)) shows a 5 K increase in transformation temperatures.

Four distinct deformation stages can be identified in the stress-strain curves for both uniaxial quasi-static ( $10^{-3} \text{ s}^{-1}$ ) and dynamic high-rate ( $1500 \text{ s}^{-1}$ ) compression as illustrated in Figure 5. Within Stage I, samples deform linear-elastically as strain increases up to ~0.5 pct strain for both quasi-static and dynamic compression. While both samples exhibited an elastic modulus of about 32 GPa which is within the range of elastic moduli values reported in the literature,<sup>[15,52,55]</sup> there does appear to be some slight deviation from linearity in the dynamic compression curve in Stage I. After about 0.8 pct, the onset of the stress plateau was observed (Stage II), where the stress in the specimen increases less prominently with increasing strain. The stress plateau of the quasi-static compression experiment continues to about 2.5 pct strain, while the stress plateau of the dynamic compression experiment ends more gradually between 3 and 4 pct strains. Like in Stage I, the change between Stage II to III in the dynamic compression experiment is less distinct due to the heterogeneous nature of deformation during dynamic loading likely

resulting in both martensite reorientation and martensite elasto-plastic deformation, the latter being less present in the quasi-static compression experiment.<sup>[45]</sup> The change in slope is markedly different in Stage III between the quasi-static and dynamic compression experiments, where the slope of the dynamic compression experiment is much steeper (48.9 GPa) as compared to the quasi-static compression experiment (26.5 GPa). The point at which the quasi-static compression sample reaches Stage IV appears to be at around 1170 MPa (6 pct strain) and continues in Stage IV to about 1550 MPa (9.5 pct strain) before unloading. It is likely that the slope for the dynamic compression experiment is a combination of both elastic and plastic deformation during Stage III. The dynamic compression sample enters Stage IV at about 1770 MPa (6.9 pct strain), which is above the yield stress of martensite and continues to about 2 GPa (8.5 pct strain) before unloading occurs.

#### IV. DISCUSSION

The morphological features of martensitic NiTi before and after dynamic compression are shown in Figure 6. Comparing the SEM images from the same location of the same specimen, the surface of the sample after dynamic deformation has a rougher, more corrugated texture than that of the surface of the sample before any deformation. As illustrated in Figure 6(b), microcracks can be seen in  $\text{Ti}_2\text{Ni}$  particles, especially the larger sized particles, after dynamic compression. The microcracks extend through the particles and terminate at the boundary between the particle and the matrix. In contrast to the relatively ductile soft NiTi matrix,  $\text{Ti}_2\text{Ni}$  particles are inherently hard and brittle and, thus, more readily fracture at high stress levels.

SEM images of triple junctions in NiTi SMA samples (a) before compression, (b) after quasi-static compression, and (c) after dynamic compression are shown in Figures 7(a) through (c), respectively. Before compression in the as-received hot-rolled state (Figure 7(a)), grain size is on the order of 10  $\mu\text{m}$ , as shown in Figure 2, with martensite variant widths, which span whole grains, on the order of 200 nm. Grain boundaries can be clearly seen as well as typical well-ordered and aligned martensite variants within the grains. After quasi-static compression (Figure 7(b)), primary martensite variant widths, which span whole grains, have become smaller on the order of 100 nm with even smaller secondary martensite variants in between the primary variants on the order of 50 nm. Grain boundaries and triple junctions can still be easily identified; however, the initial martensite variants have transformed into smaller variants which align in a preferred direction. After dynamic compression (Figure 7(c)), the grain size is difficult to determine because the grain boundaries have become difficult to clearly distinguish due to severe deformation. The primary martensite variant widths no longer span whole grains and have become fragmented; however their spacing is much more variable and much smaller on the order of ~50 nm.

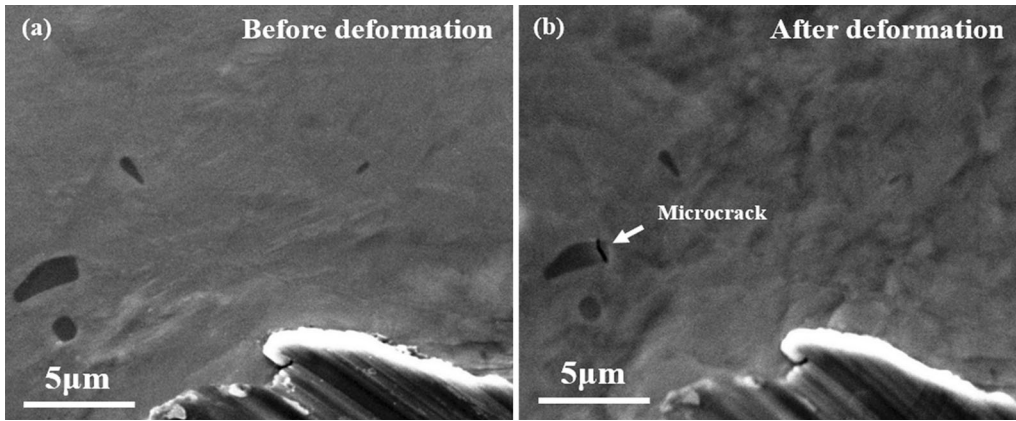


Fig. 6—SEM images of martensitic NiTi (a) before dynamic compression and (b) after dynamic compression.

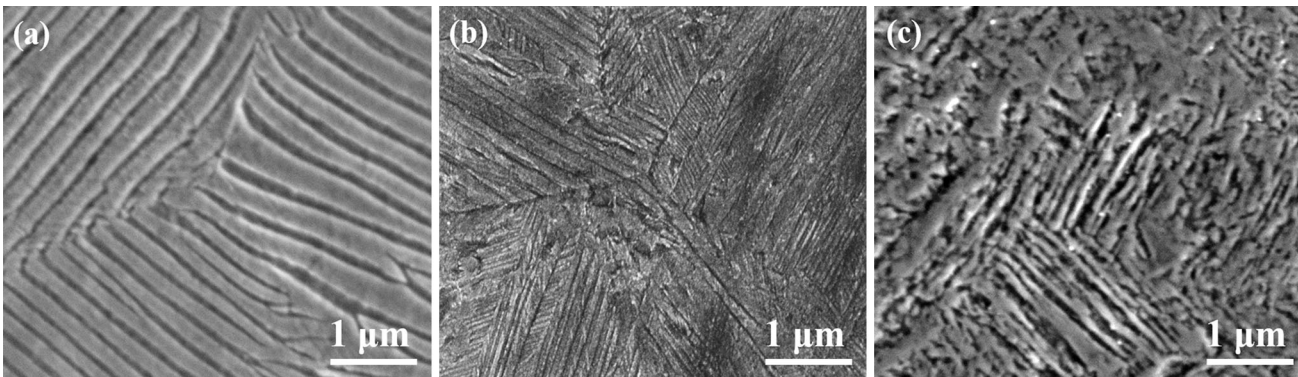


Fig. 7—SEM images of martensitic NiTi (a) before compression, (b) after quasi-static compression (strain rate:  $10^{-3} \text{ s}^{-1}$  and strain 10 pct), and (c) after dynamic compression (strain rate:  $1500 \text{ s}^{-1}$  and strain 9 pct).

Grain boundaries and triple junctions are difficult to distinguish too. During dynamic compression, the initial variants deform at such a high rate that they are unable to reduce the strain by martensitic reorientation; instead the original variants intersect each other, overlap, and blur the grain boundaries.

As illustrated in Figure 5, the softening of the slope in the elastic region (Stage I) is due to the influence of martensitic reorientation in combination with elastic deformation. The change in slope (or stress plateau) in Stage II (Figure 5) is due to localized Lüders-like martensitic reorientation to accommodate variants in preferred directions, which is often in the direction of the applied stress.<sup>[56,57]</sup> During quasi-static compression, not all of the martensite variants reorient within Stage II, and so the slope in Stage III is less steep since martensite reorientation continues to occur along with elastic deformation of the reoriented martensite as the strain increases. In contrast, during dynamic compression, more of the martensite variants reorient within in Stage II extending this region by about 1.2 pct more strain before the slope in Stage III becomes much more abrupt and exhibits a steeper slope.

Figure 8 shows X-ray diffraction (XRD) patterns of martensitic NiTi samples (a) before compression, (b) after dynamic compression, (c) after quasi-static compression, (d) after dynamic compression and annealing

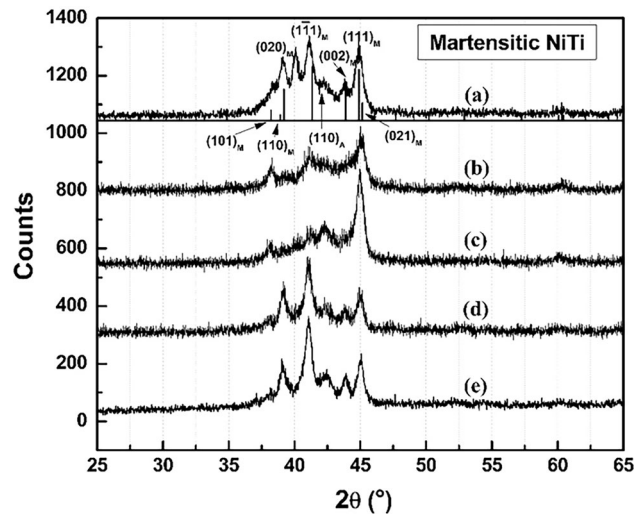


Fig. 8—Comparison of XRD patterns (a) before compression, (b) after dynamic compression, (c) after quasi-static compression, (d) after dynamic compression and annealing at 873 K (600 °C) for 30 min, and (e) after quasi-static compression and annealing at 873 K (600 °C) for 30 min.

at 873 K (600 °C) for 30 minutes, and (e) after quasi-static compression and annealing at 873 K (600 °C) for 30 minutes. The sample before compression shows

diffraction peaks from monoclinic martensitic NiTi (PDF#: 00-035-1281<sup>[58]</sup>) and cubic austenitic NiTi (PDF#: 00-019-0850<sup>[59]</sup>). While Ti<sub>2</sub>Ni particles are observed in the SEM images, the Ti<sub>2</sub>Ni phase (PDF#: 00-018-0898<sup>[60]</sup>) is not detectable using XRD likely due to the fact that only a small percentage of the particles are present, and therefore, the intensity of the diffraction is weak. The sample before compression is predominantly martensitic as evident from the intensities of the (101)<sub>M</sub>, (020)<sub>M</sub>, (111)<sub>M</sub>, (002)<sub>M</sub>, (111)<sub>M</sub> planes of martensitic NiTi in Figure 8; however, a small amount of austenite is also observable, while R-phase was not observed in X-ray diffraction patterns due to its instability at room temperature, at which the XRD was carried out. If R-phase was present, the six most intense peaks within a 2θ range of 25–65 deg would be located at a 2θ (normalized intensity) of 29.6 deg (6.7), 42.1 deg (100), 44.5 deg (3.8), 61.4 deg (26.5), 76.6 deg (8.8), and 77.6 deg (19.1).<sup>[61]</sup> While it is not possible to resolve R-phase in XRD, according to the DSC results in Figure 4, the peak which appears before the austenite peak during cooling is typical of R-phase and is assumed to be R-phase here.<sup>[13,53,54]</sup> All peak intensities from the NiTi sample after dynamic compression have decreased, indicating that accommodation has occurred and that many of the martensite grains have reoriented to the (101)<sub>M</sub>, (111)<sub>M</sub>, and (111)<sub>M</sub> planes. The sample after quasi-static compression exhibits a similar behavior; however, the intensity from the (111)<sub>M</sub> plane is much stronger, which is in alignment with the SEM images from samples after quasi-static compression. Therefore, most of crystal planes align in [111]<sub>M</sub> direction after both dynamic and quasi-static loading, which is likely the loading direction and drawing direction. After annealing at 873 K (600 °C) for 30 minutes, samples after both quasi-static and dynamic compression show an increase in the intensities of the (002)<sub>M</sub> and (111)<sub>M</sub>, a return of the (002)<sub>M</sub> plane, and a decrease in the intensity of the (111)<sub>M</sub> plane. Annealing the samples results in relaxation of the strained regions which allows for reoriented martensite to return to its original martensite variants.

The XRD pattern change can be explained by the Scherrer equation<sup>[62,63]</sup>:

$$\beta = \frac{K\lambda}{L \cos \theta},$$

where λ is the wavelength of the incident X-ray, K is a constant and equal to 0.94 under two basic assumptions, Gaussian line type behavior and the particles have a homogeneous cubic shape, L is the crystallite size, and θ is the diffraction angle, β is the line broadening at half the maximum intensity (FWHM) in radians. Peak broadening (Figure 8) and a decrease in FWHM, according to the Scherrer equation, indicate that more strain is present in a given orientation due to small distortions of the lattice after both dynamic and quasi-static compression. Under dynamic compression, greater reorientation can be seen in Figure 7(c), where grain

boundaries and primary and secondary martensite variants can be clearly identified after quasi-static compression; however, the grain boundaries are difficult to distinguish and only some of the martensite variants can be found after dynamic compression. This also can be seen by comparing the intensities of (101)<sub>M</sub>, (020)<sub>M</sub>, (111)<sub>M</sub>, (002)<sub>M</sub>, and (111)<sub>M</sub> crystal planes of martensitic NiTi after dynamic compression and quasi-static compression.

## V. CONCLUSIONS

The mechanical behavior, microstructural changes, and phase transformation behavior of martensitic NiTi SMAs were examined in the as-received hot-rolled state and after annealing at various times and temperatures under quasi-static and dynamic compression. Several conclusions are drawn upon the results:

1. Phase transformation peaks disappear after quasi-static and dynamic compression. This result indicates that the shape memory effect has been completely removed due to the large amount of plastic deformation that occurs during dynamic compression. Subsequent annealing at 1123 K (850 °C) for 30 minutes results in the reappearance of the shape memory effect with a more distinct two-step phase transformation (M→R, R→A). It is interesting to note, however, that the material can be completely recovered by annealing at 873 K (600 °C) for 30 minutes.
2. The stress-strain curve under dynamic compression showed a longer stress plateau and a higher plastic stress level in the plastic deformation region as compared to that under quasi-static compression. This is likely due to a more complete reorientation of martensite occurring before Stage III (elastic deformation of reorientated martensite), under dynamic loading, while martensite reorientation extends and continues into elastic deformation of reorientated martensite region under quasi-static loading.
3. As indicated by XRD, residual strain after unloading shows that the intensities of most diffraction peaks decrease after both dynamic and quasi-static compression, with the exception of (111)<sub>M</sub> plane which remains essentially constant or even increases after quasi-static loading, which indicates the preferred martensitic direction. The relaxation of strained regions during annealing enhances the recovery of reoriented martensite variants; consequently, the return of the shape memory effect is observed.

Based on our results, martensitic NiTi SMAs show excellent properties as damping materials at both quasi-static and dynamic compression. They both exhibit about the same amount of stored energy, which can be fully recovered at strains below ~6 pct.

## ACKNOWLEDGMENTS

This research was financially supported by startup funds of Dr. Xu Nie and Dr. Marcus L. Young. Dr. Xu Nie also thanks to the Air Force Research Laboratory (AFRL/RW) for partial financial support under Agreement Number FA8651-14-2-0007. The authors would like to thank Scott Schlegel (ATI Specialty Alloys and Components, Albany, Oregon) and Brian Van Doren (Specialty Alloys and Components, Albany, Oregon) for useful discussions. NiTi SMA rods were supplied by ATI Specialty Alloys and Components, Albany, Oregon. The authors would like to acknowledge the Center for Advanced Research and Technology at University of North Texas for access to the experimental facilities used for this study.

## REFERENCES

1. L. Janke: *Mater. Struct.*, 2005, vol. 38 (279), pp. 578–92.
2. G. Song, N. Ma, and H.N. Li: *Eng. Struct.*, 2006, vol. 28 (9), pp. 1266–74.
3. J. Van Humbeeck: *Mater. Sci. Eng. A*, 1999, vol. 273, pp. 134–48.
4. T.W. Duerig, A. Pelton, and D. Stöckel: *Mater. Sci. Eng. A*, 1999, vol. 273, pp. 149–60.
5. L.G. Machado and M.A. Savi: *Braz. J. Med. Biol. Res.*, 2003, vol. 36 (6), pp. 683–91.
6. L. Petrini and F. Migliavacca: *J. Metall.*, 2011, vol. 2011, pp. 1–15.
7. N.B. Morgan: *Mater. Sci. Eng. A*, 2004, vol. 378 (1–2), pp. 16–23.
8. A. Biscarini, G. Mazzolai, and A. Tuissi: *Recent Pat. Biomed. Eng.*, 2008, vol. 1 (3), pp. 180–96.
9. O. Benafan, J. Brown, F.T. Calkins, P. Kumar, A.P. Stebner, T.L. Turner, R. Vaidyanathan, J. Webster, and M.L. Young: *Int. J. Mech. Mater. Des.*, 2013, vol. 10 (1), pp. 1–42.
10. E.T.F. Chau, C.M. Friend, D.M. Allen, J. Hora, and J.R. Webster: *Mater. Sci. Eng. A*, 2006, vols. 438–440, pp. 589–92.
11. D.J. Hartl, D.C. Lagoudas, F.T. Calkins, and J.H. Mabe: *Smart Mater. Struct.*, 2010, vol. 19 (1), p. 015020.
12. K. Otsuka and X. Ren: *Intermetallics*, 1999, vol. 7 (5), pp. 511–28.
13. K. Otsuka and X. Ren: *Prog. Mater. Sci.*, 2005, vol. 50 (5), pp. 511–678.
14. K. Otsuka and C.M. Wayman: *Shape Memory Materials*, Cambridge University Press, Cambridge, 1999.
15. M.L. Young, M.F.X. Wagner, J. Frenzel, W.W. Schmahl, and G. Eggeler: *Acta Mater.*, 2010, vol. 58 (7), pp. 2344–54.
16. J. Ryhänen, E. Niemi, W. Serlo, E. Niemelä, P. Sandvik, H. Pernu, and T. Salo: *J. Biomed. Mater. Res.*, 1997, vol. 35 (4), pp. 451–57.
17. S.A. Shabalovskaya: *Bio-Med. Mater. Eng.*, 2002, vol. 12 (1), pp. 69–109.
18. L. Tan: *Biomaterials*, 2003, vol. 24 (22), pp. 3931–39.
19. C.P. Frick, A.M. Ortega, J. Tyber, A. El M. Maksound, H.J. Maier, Y. Liu, and K. Gall: *Mater. Sci. Eng. A*, 2005, vol. 405 (1–2), pp. 34–49.
20. Y. Liu and P.G. McCormick: *Acta Metall. Mater.*, 1994, vol. 42 (7), pp. 2401–06.
21. J.A. Shaw and S. Kyriakides: *J. Mech. Phys. Solids*, 1995, vol. 43 (8), pp. 1243–81.
22. S. Mändl, D. Krause, G. Thorwarth, R. Sader, F. Zeilhofer, H.H. Horch, and B. Rauschenbach: *Surf. Coat. Technol.*, 2001, vol. 142, pp. 1046–50.
23. P. Sevilla, F. Martorell, C. Libenson, J.A. Planell, and F.J. Gil: *J. Mater. Sci. Mater. Med.*, 2008, vol. 19 (2), pp. 525–29.
24. E. Choi, Y. Chung, J. Choi, H. Kim, and H. Lee: *Smart Mater. Struct.*, 2010, vol. 19 (3), p. 035024.
25. M. Frotscher, J. Burow, P. Schön, K. Neuking, R. Böckmann, and G. Eggeler: *Materialwiss. Werkstofftech.*, 2009, vol. 40 (1–2), pp. 17–22.
26. B. Kockar, I. Karaman, J.I. Kim, and Y. Chumlyakov: *Scripta Mater.*, 2006, vol. 54 (12), pp. 2203–08.
27. J.L. Lemanski, V.B. Krishnan, R.M. Manjeri, W.U. Notardonato, and R. Vaidyanathan: *Advances in Cryogenic Engineering*, AIP Publishing, Melville, 2006, pp. 3–10.
28. D.A. Miller and D.C. Lagoudas: *Smart Mater. Struct.*, 2000, vol. 9 (5), p. 640.
29. S. Nemat-Nasser, J.Y. Choi, W. Guo, J.B. Isaacs, and M. Taya: *J. Eng. Mater. Technol.*, 2005, vol. 127 (1), p. 83.
30. S. Nemat-Nasser and W. Guo: *Mech. Mater.*, 2006, vol. 38 (5–6), pp. 463–74.
31. S. Nemat-Nasser, J. Choi, W. Guo, and J.B. Isaacs: *Mech. Mater.*, 2005, vol. 37 (2–3), pp. 287–98.
32. W. Chen and S. Bo: *J. Mech. Mater. Struct.*, 2006, vol. 1 (2), pp. 339–56.
33. B. Song: *Exp. Mech.*, 2004, vol. 44 (6), pp. 622–27.
34. S.P. Belyaev, N.F. Morozov, A.I. Razov, A.E. Volkov, L. Wang, S. Shi, S. Gan, J. Chen, and X. Dong: *Materials Science Forum*, Trans Tech Publications, Dürnten, 2002, pp. 337–40.
35. W. Guo, J. Su, Y. Su, and S.Y. Chu: *J. Alloys Compd.*, 2010, vol. 501 (1), pp. 70–76.
36. W. Chen, Q. Wu, J.H. Kang, and N.A. Winfree: *Int. J. Solids Struct.*, 2001, vol. 38 (50), pp. 8989–98.
37. R.R. Adharapurapu, F. Jiang, K.S. Vecchio, and G.T. Gray: *Acta Mater.*, 2006, vol. 54 (17), pp. 4609–20.
38. H. Date: *Materials Science Forum*, Trans Tech Publications, Dürnten, 2007, p. 3231.
39. A. Bragov, A. Galieva, V. Grigorieva, A. Danilov, A. Konstantinov, A. Lomunov, A. Motorin, E. Ostropiko, and A. Razov: *Materials Science Forum*, Trans Tech Publications, Dürnten, 2013, pp. 326–31.
40. J. McCormick and R. DesRoches: *Proceedings of the 2004 Structures Congress*, 2004, pp. 22–26.
41. R. DesRoches and M. Delemont: *Eng. Struct.*, 2002, vol. 24 (3), pp. 325–32.
42. J. Frenzel, E.P. George, A. Dlouhy, C. Somsen, M.F.X. Wagner, and G. Eggeler: *Acta Mater.*, 2010, vol. 58 (9), pp. 3444–58.
43. Y. Liu, Y. Liu, and J. Van Humbeeck: *Acta Mater.*, 1998, vol. 47 (1), pp. 199–209.
44. Z. Xie, Y. Liu, and J. Van Humbeeck: *Acta Mater.*, 1998, vol. 46 (6), pp. 1989–2000.
45. Y. Liu, Z. Xie, J. Van Humbeeck, and L. Delaey: *Acta Mater.*, 1998, vol. 46 (12), pp. 4325–38.
46. I. Karaman, H.E. Karaca, Z.P. Luo, and H.J. Maier: *Metall. Mater. Trans. A*, 2003, vol. 34A, pp. 2527–39.
47. Y. Liu, Y. Li, K.T. Ramesh, and J. Van Humbeeck: *Scripta Mater.*, 1999, vol. 41 (1), pp. 89–95.
48. H. Nakayama, Y. Zhao, M. Taya, W.W. Chen, Y. Urushiyama, and S. Suzuki: *Smart Structures and Materials*, International Society for Optics and Photonics, Orlando, 2005, pp. 355–63.
49. Y. Liu, Y. Li, and K.T. Ramesh: *Philos. Mag. A*, 2002, vol. 82 (12), pp. 2461–73.
50. Y. Liu, J. Van Humbeeck, R. Stalmans, and L. Delaey: *J. Alloys Compd.*, 1997, vol. 247 (1), pp. 115–21.
51. X. Huang and Y. Liu: *Scripta Mater.*, 2001, vol. 45 (2), pp. 153–60.
52. Y. Liu and H. Xiang: *J. Alloys Compd.*, 1998, vol. 270 (1), pp. 154–59.
53. P. Šittner, M. Landa, P. Lukáš, and V. Novak: *Mech. Mater.*, 2006, vol. 38 (5), pp. 475–92.
54. J.I. Kim, Y. Liu, and S. Miyazaki: *Acta Mater.*, 2004, vol. 52 (2), pp. 487–99.
55. T. Sakuma, Y. Mihara, H. Toyama, Y. Ochi, and K. Yamauchi: *Mater. Trans.*, 2006, vol. 47 (3), p. 787.
56. P. Šittner, Y. Liu, and V. Novak: *J. Mech. Phys. Solids*, 2005, vol. 53 (8), pp. 1719–46.
57. K.N. Melton and O. Mercier: *Acta Metall.*, 1981, vol. 29 (2), pp. 393–98.
58. G.M. Michal and R. Sinclair: *Acta Crystallogr. Sect. B.*, 1981, vol. 37 (10), pp. 1803–07.
59. H. Hughes: *J. Iron Steel Inst.*, 1965, vol. 203 (10), pp. 1019–23.
60. G.A. Yurko, J.W. Barton, and J. Gordon Parr: *Acta Crystallogr.*, 1959, vol. 12 (11), pp. 909–11.
61. T. Goryczka and H. Morawiec: *J. Alloys Compd.*, 2004, vol. 367 (1), pp. 137–41.
62. P. Scherrer: *Nachrichten von der Gesellschaft der Wissenschaften zu Göttingen, mathematisch-physikalische Klasse*, 1918, vol. 1918, pp. 98–100.
63. A. Patterson: *Phys. Rev.*, 1939, vol. 56 (10), pp. 978–82.